Thermal holographic patterns for ultrasound hyperthermia

Diana Andrés, Jonathan Vappou, Noé Jimenez, Francisco Camarena

Thermal holographic patterns for ultrasound hyperthermia

Diana Andrés,[1] Jonathan Vappou,[2] Noé Jiménez,[1] and Francisco Camarena[1]
[1)]*Instituto de Instrumentación para Imagen Molecular (i3M), Universitat Politècnica de València, Consejo Superior de Investigaciones Científicas (CSIC), Valencia, Spain*
[2)]*Université de Strasbourg, Centre National de la Recherche Scientifique (CNRS), ICube, UMR7357, Strasbourg, France*

(*Electronic mail: nojigon@upv.es, corresponding author.)

(Dated: 9 December 2021)

Holograms can shape wavefronts to produce arbitrary acoustic images. In this work, we experimentally demonstrate how acoustic holograms can produce controlled thermal patterns in absorbing media at ultrasonic frequencies. MRI-compatible holographic ultrasound lenses were designed by time-reversal methods and manufactured using 3D-printing. Several thermal holographic patterns were measured using MRI thermometry and a thermographic camera in both gelatin-milk phantoms and ex-vivo cow-liver tissue. The results show that acoustic holograms enable spatially-controlled heating in arbitrary regions. Rising the temperature using low-cost and MRI-compatible holographic transducers might be of great interest for many biomedical applications, such as ultrasound hyperthermia, where the control of specific thermal patterns is needed.

Optical holograms can modulate light wavefronts to generate visible images[1]. In the same way, acoustic images can also be synthesized by holograms, shaping the areas where mechanical waves present a high amplitude, and areas where the matter is at rest. Holographic acoustic fields can be synthesized by ultrasound phased-array systems[2,3], but the small number of active radiating elements, typically up to one thousand, limits its performance. In addition, the cost associated to these systems in terms of driving electronics and independent impedance matching makes them unaffordable for many applications. In recent years, acoustic holograms have been exhaustively studied[4], mainly triggered by the emergence of 3D printing technologies. Artificially-structured materials, such as complex phase plates[4,5] (also known as kinoforms[6]), gratings[7,8], or metamaterials[9–12], have enabled accurate wavefront engineering for many applications such as particle trapping and manipulation[13,14], scattering control and vortex generation[15], fast 3D-printing[16], volumetric displays[17] or 3D imaging[18].

Compared to light, acoustic waves can penetrate much deeper into biological media. Therefore, acoustic holograms are bursting onto current biomedical applications due to their capability to shape and focus ultrasound fields inside living tissues. Acoustic holograms can encode complex wavefronts compensating the phase aberrations produced by stiff layers of tissues, such as skull bones in transcranial propagation, enabling the creation of single focal spots[19], arbitrary therapeutic patters in the brain[20,21], or even vortex beams[22]. Other recent uses of acoustic holograms in biomedical applications include cell patterning[23], the control of cavitation patterns, that has been demonstrated in homogeneous tissue phantoms with embedded microbubbles[24] and in-vivo inside the head of small animals[25], or burst-wave lithotripsy[26].

Acoustic waves transport energy, and when propagating into biological media a fraction is irreversibly transformed into heat by viscoelastic and relaxation processes. In ultrasound imaging applications the temperature rise is negligible because the total energy of the wave is moderate[27]. However, at high ultrasound intensities heat deposition can be elevated and fast enough to create cell necrosis and tissue ablation[28]. Combined with sharp focusing, high intensity focused ultrasound is currently used in clinics for therapeutical purposes[29]. Recently, attention has been paid to intermediate regimes, when ultrasound is used to create a local and mild hyperthermia, which is defined as a rise in tissue temperature between 39° C and 45° C, typically with long exposure times[30,31,33]. HIFU-mediated hyperthermia is emerging as a highly promising therapeutic approach that has been shown to activate the immune system, and/or enhance drug delivery, in particular for chemotherapeutic drug administration[32,34]. Usually in mild hyperthermia applications a wide region of tissue is covered sequentially by multiple focal spots, by using the electronic steering of the beam of a phased-array transducer,which is in fact an active research topic[35–37]. During treatment, the temperature inside the tissue is monitored using magnetic resonance imaging (MRI) thermometry, resulting in long treatment duration and expensive MRI-compatible devices.

In this work, we demonstrate how acoustic holograms can create arbitrary thermal patterns in ex-vivo biological media and tissue-mimicking phantoms using a low-cost MRI compatible transducer, resulting in a portable, patient-specific and personalized therapeutical device. We illustrate the concept using two target holographic patterns. First, an arbitrary thermal image is produced, and, second, we enlarge the thermal pattern of an ultrasound device currently used for hyperthermia applications using a holographic lens. For the first configuration, the target thermal pattern has the shape of the number "2". For this configuration we use a flat piezoelectric disc of aperture $2a = 50$ mm and central frequency $f_0 = 1.1$ MHz, mounted on a 3D-printed MRI-compatible custom-design housing. For the second configuration, we use a commercial spherically-focused ultrasound transducer of radius of curvature $F = 100$ mm, elliptical aperture of mayor axis $2a = 125$ mm and $b = 85$ mm, and central frequency of $f_0 = 1$ MHz.

Acoustic holograms were designed using time reversal methods, following the procedure described by Jiménez-Gambín *et al.* [20]. First, an array of virtual sources were dis-

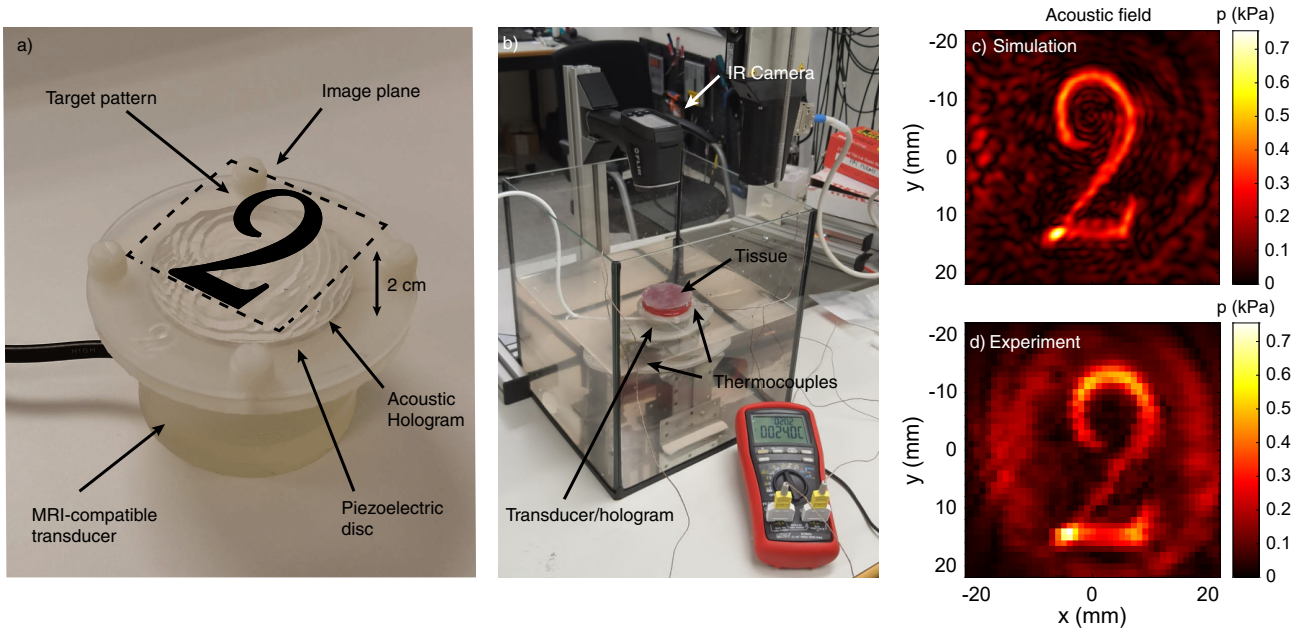

FIG. 1. (a) MRI-compatible transducer and holographic lens. (b) Experimental setup for thermal measurements. (b) Simulated acoustic pressure field. (c) Acoustic pressure field measured in degassed water.

tributed in the area corresponding to the shape of the target image, e.g., the number "2". Each source was set to emit a 100-cycles sinusoidal tone burst at the transducer working frequency, with the same amplitude and a relative phase proportional to the distance from the virtual source to the transducer surface as e^{ikz}. The simulated medium was homogeneous with the acoustic and thermal properties matching those of a liver tissue. Density and sound speed values were set to $\rho_t = 1079$ kg/m^3 and $c_t = 1586$ m/s, respectively[38,39]. Acoustic attenuation follows a frequency power-law given by $\alpha_t = \alpha_0 f^\gamma$, where f is the frequency, and for liver tissue $\gamma = 1.1$ and α_0 was set to obtain an attenuation of 0.59 dB/(cm·MHz$^\gamma$). The wavefront generated by the interference of the sound waves coming from each virtual source is captured in a plane parallel to the transducer surface, the holographic surface, which is divided into squared pixels of side 0.25 mm. The acoustic hologram is composed of elastic columns, acting as acoustic Fabry-Perot resonators, and each one corresponding to a pixel of the holographic surface. By tuning the height of each column the transmission coefficient can be spatially-modulated. In this way, the transmitted field was set to mimic a phased-conjugated version of the recorded wavefront[20]. We fix a minimal lens thickness of 2.5 mm, which corresponds to $7\lambda/4$ in liver medium, for mechanical robustness when 3D-printing. Maximum lens height is 5.45 mm, so the resulting lens was approximately a flat disc with a roughness of about 3 mm, see Fig. 1 (a). Lenses were 3D printed using stereolithographic methods on a photosensitive resin (Clear resin, Formlabs, USA), printed on a 50 μm resolution printer (Form 2, Formlabs, USA). The density and sound-speed values of the lens were experimentally obtained as $\rho_L = 1171$ kg/m^3, $c_L = 2580$ m/s, respectively. Attenuation was set to 2.72 dB/(cm·MHz$^\gamma$), according to previously reported values for similar photopolymers[4].

The resulting pressure fields were validated by simulations using a pseudo-spectral time-domain method[40], and by experimental measurements of the acoustic field, the latter performed in a degassed water tank at 23° C maintained by a water conditioning unit (WCU-Series, Sonic Concepts, USA). The flat holographic lens was directly coupled to the custom-made MRI-compatible piezoelectric transducer as shown in Fig. 1 (a). Acoustic field measurements were performed using a piezoelectric hydrophone (-225.5 dB re 1 V/μPa at 1 MHz, Model Y-104, Sonic Concepts, USA), calibrated from 40 kHz to 2 MHz, attached to a 3D positioning system (5 μm precision, PI Micos GmbH, Germany). The transducer was driven by a 20-cycles sinusoidal pulse burst at a frequency of $f = 1.1$ MHz using a signal generator (14 bits, 100 MS/s, model PXI5412, National Instruments, USA) and amplified by a linear RF amplifier (ENI 1040L, 400 W, 55 dB, ENI, Rochester, NY, USA). The acoustic signals were recorded scanning a plane at $z = 20$ mm, from -22 mm $< x <$ 22 mm and -22 mm $< x <$ 22 mm, using steps of 1 mm. Signals were averaged 20 times at each location to reduce random noise. The resulting simulated and experimental acoustic field is presented in Figs. 1 (c, d), respectively. Experimental acoustic field is in good agreement with the simulated one. Discrepancies between the two pressure fields might be related to the fact that the holographic lens was designed for a liver-like medium but measured in water, which exhibits slightly different properties in terms of acoustic impedance and sound speed. Measured peak-pressure reaches 0.7 kPa at the brightest spot of the image.

Volume rate of heat deposition in liver tissue is given by the quantity $Q = 2\alpha_t I$, where α_t is the tissue absorption coefficient and $I = p^2/2\rho_t c_t$ is the acoustic intensity, calcu-

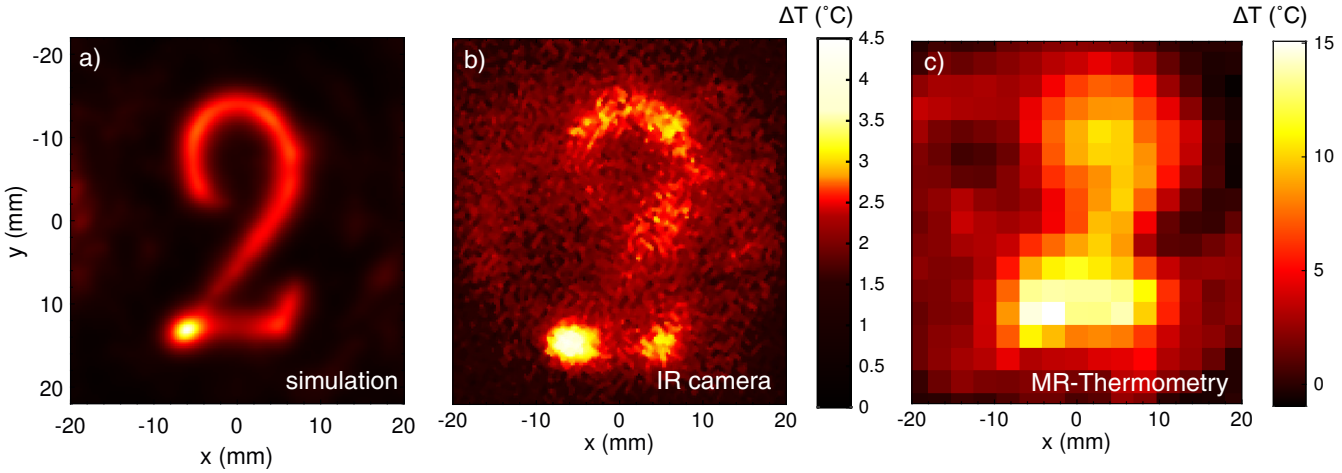

FIG. 2. (a) Simulated thermal pattern in liver tissue after 12 seconds heating. (b) Thermal pattern measured with an infrared camera in liver tissue after 12 seconds heating and (c) measured with MR-thermometry after 40 seconds heating. The central vertical colour scale applies to (a) and (b).

lated using the peak pressure value at the steady state of the acoustic simulation. Thermal holographic pattern is obtained by a time-domain numerical solution of the Penne's bio-heat equation[41], using a pseudo-spectral time-domain method, given by

$$\rho_t C_t \frac{\partial T}{\partial t} = \nabla(\kappa \nabla T) - W_b C_b (T - T_a) + Q, \qquad (1)$$

where T is the tissue temperature, ρ_t and C_t are the tissue density and specific heat capacity, W_b is the blood perfusion rate, C_b is the blood specific heat capacity, T_a is the blood ambient temperature and κ is the tissue thermal conductivity. We have not considered blood perfusion ($W_b = 0$) to mimic the conditions of the ex-vivo experiment. Specific heat capacity and thermal conductivity were set to $C_t = 3540$ J/(kg·K) and $k = 0.52$ W/(m·K), according to values reported for liver tissue[38]. Thermal simulation and experiments were carried out by driving the source with a continuous sinusoidal signal at its central frequency (f_0 = 1.1 MHz). Experimental validation was performed using two systems. On the one hand, temperature was measured with an infrared thermal camera (Testo 365, Testo, Germany) at the surface of a 20-mm slice of degassed cow liver tissue, taking images at a rate of 15 frames per minute. On the other hand, temperature was measured by proton-resonance frequency-shift (PRFS) MR-thermometry using a 1.5 T Aera MRI (Siemens, Erlangen, Germany). A single-slice using a 2D gradient-echo (GRE) sequence was used for MR-PRFS thermometry, obtaining one thermal image every 1.2 seconds[42].

Because IR radiation is strongly absorbed by water, IR-camera measurements were performed at the tissue surface, with the image plane located at the boundary between the soft-tissue and the air. Note that when using this setup ultrasound waves are strongly reflected at the boundary, because the impedance mismatch produces a nearly-perfect Neumann boundary condition for the pressure at the image plane. Even in these conditions, the target thermal pattern is observed, as Fig. 2 (b) shows. The pattern matches the simulated one (Fig. 2 (a)), with a peak temperature rise of $\Delta T = 4.5^\circ$ C after 12 seconds heating at 20 W. The temperature was measured locally by two thermocouples located in the water tank and at the lateral boundary of the tissue (see Fig. 1 (b)), indicating that diffusion transports heat towards the boundary of the tissue in the long term, and the pattern becomes blurred[43]. The concept was also validated in the bulk of a liver-mimicking gelatin-milk phantom using MRI-thermometry to minimize the influence of the previously-mentioned boundary condition. The measured thermal pattern using MRI at the image plane is presented in Fig. 2 (c). HIFU heating was performed at 40 W acoustic power, leading to a temperature rise of $\Delta T = 15^\circ$ C after 40 seconds of heating. Both experiments demonstrate that the desired thermal pattern can be generated using holograms, showing the robustness of acoustic holograms to generate thermal patterns inside absorbing media. In both cases the thermal pattern is well defined until heat diffusion dominates and the central part of the hologram is almost uniformly heated, as it also occurs in simulations[44].

Ultrasound hyperthermia treatments may require extended volumes in which temperature should increase a few degrees. For this application, in addition to the possible need for a complex thermal pattern as illustrated in the previous example, it may be of great interest to cover a wide target area with a uniform temperature distribution, e.g., a tumour. Therefore, it might be desired to widen and shift axially the narrow focal spot of a focused ultrasound source, with the aim of matching the thermal pattern to a target area of therapeutical interest. In this way, a second hologram was designed to enlarge and shift the natural focus of a spherically-focused commercial transducer (Imasonic, Voray sur l'Ognon, France), shown in Fig. 3 (a). The desired region in which temperature should increase was defined as an ellipse with 15-mm width and 10-mm height dimensions, located at a depth of 65 mm from the transducer surface. Thermal patterns were computed with k-space numerical simulations. Experimentally, temperature was measured using MR-thermometry in a liver-mimicking phantom, driving the source with a 1 MHz continuous signal at 80 W

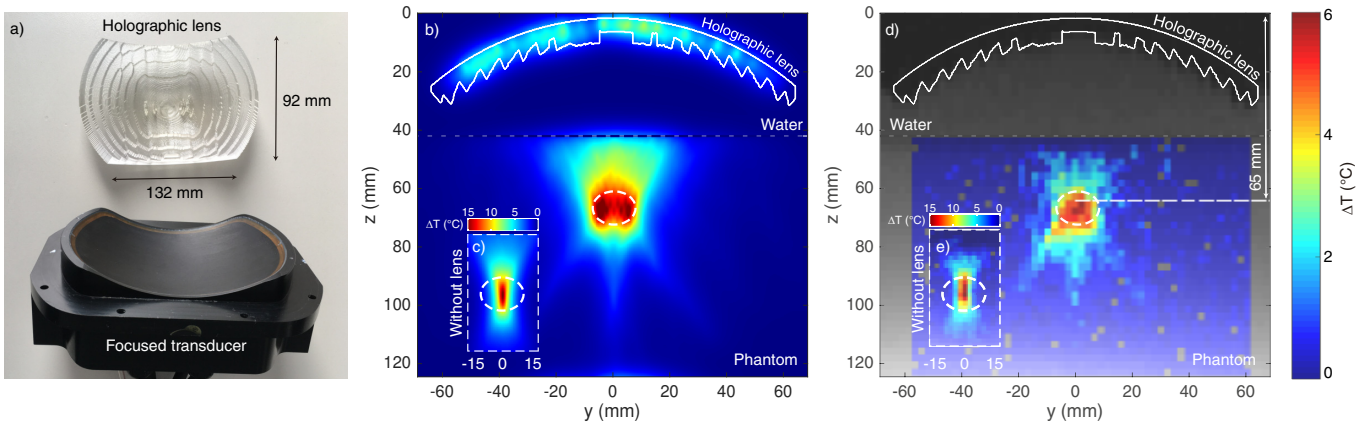

FIG. 3. (a) Acoustic hologram and focused transducer for the second experimental setup. (b) Thermal simulation for a 1-cm wide hologram located at 65 mm from the focused transducer surface and (c) for the focused transducer without the lens. (d) MRI-thermometry measurement using the hologram and (e) for the focused transducer without the lens. The big vertical colour scale applies to (b) and (d).

acoustic power without the lens and 200 W with the holographic lens[45]. The resulting patterns are shown in Figs. 3 (b-e). A temperature rise of $\Delta T = 6^\circ$ C was observed in both simulation and MRI measurement of the system with lens after 30 seconds heating, while for the transducer-only setup the temperature rise was of $\Delta T = 15^\circ$ C in the same time. A good agreement is found between simulations [Figs. 3 (b, c)] and measurements [Figs. 3 (d, e)]. In the absence of the lens, a narrow focal spot of 1.5 mm wide is found, located at a depth corresponding with the centre of curvature of the source (10 cm). However, using the holographic lens the focal spot widens and shifts axially, according to the planned design. Excellent agreement was found between thermal simulations and temperature maps measured by MR-thermometry. ROIs inside which experimental temperature elevation was greater than 4 degrees were 7 mm $\times$ 25 mm and 17 mm $\times$ 16 mm without and with the holographic lens, respectively, while these same regions have 7 mm $\times$ 30 mm and 11 mm $\times$ 16 mm sizes in the experiment. In addition, note that standard deviation inside these regions were equal to 40% of the maximum temperature without the lens, but only 12% using the hologram. A detail of the thermal pattern cross-section in the lateral direction at the focal distance is shown in Figs. 4 (a,b). Data shows that a wider and more uniform heating region can be achieved using the holographic lens. Note this technology allows not only to enlarge focus size but also to change its position and length. The resulting holographic thermal pattern was widened about 2.5 times the original beam width, with a more uniform temperature distribution, and the focal distance was reduced to about the half of its original axial location.

In this work, we have demonstrated the potential of acoustic holograms to produce thermal holographic patterns inside soft tissues and tissue-mimicking phantoms. The temperature distributions were experimentally validated using infrared camera at the surface of a cow liver, and MR thermometry in the bulk of a liver-mimicking phantom. The results show that using an acoustic hologram, the heat deposition can be spatially-modulated by shaping the acoustic field. This procedure results in devices that can be easily manufactured by rapid prototyping. A complete low-cost, MR-compatible device can be achieved by combining these holographic lenses with single-element piezoelectric transducers such as the one presented in the first part of this study. In this way, patient-specific thermal patterns with tuned and uniform focal spots can be generated, using a low-cost device without the need of expensive MRI-compatible phased-array transducers. Moreover, previous works[20] have also demonstrated that acoustic holograms can also encode phase-conjugated wavefronts to mitigate the phase aberrations of layered tissues, such as bones. Therefore, thermal holographic patters could also be applied in transcranial therapy, or in any situation where aberrating layers distort the wavefront. In this way, holographic thermal patterns show a great potential for novel ultrasound hyperthermia treatments or physical therapy. They allow adapting the heating region to target therapeutical focal spots of arbitrary shape and location.

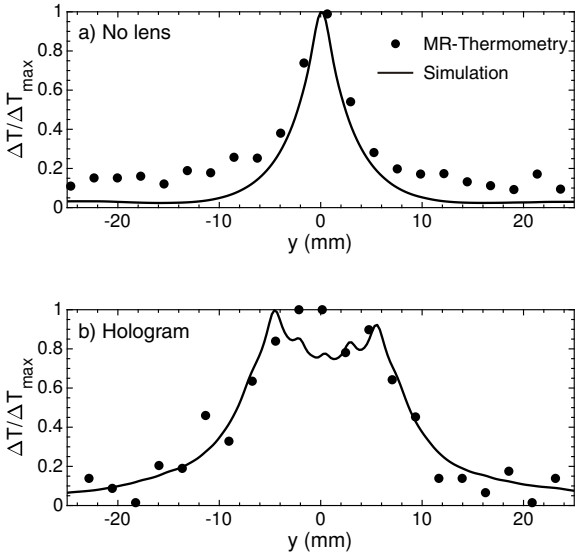

FIG. 4. Thermal pattern cross-section at the focal distance (a) in the absence of the lens and (b) including the acoustic hologram.

ACKNOWLEDGMENTS

This research has been supported by the Spanish Ministry of Science, Innovation and Universities (MICINN) through grants IJC2018-037897-I, FPU19/00601 and PID2019-111436RB-C22, by the Agència Valenciana de la Innovació through grants INNCON/2021/8 and INNVA1/2020/92, by Generalitat Valenciana through grant AICO/2020/268. Action co-financed by the European Union through the Programa Operativo del Fondo Europeo de Desarrollo Regional (FEDER) of the Comunitat Valenciana 2014-2020 (IDIFEDER/2018/022) and (IDIFEDER/2021/004). Action co-financed by BPI France, Région Grand Est and FEDER (UFOGUIDE project).

[1] D. Gabor, "A new microscopic principle," Nature **161**, 777–778 (1948).
[2] Y. Hertzberg and G. Navon, "Bypassing absorbing objects in focused ultrasound using computer generated holographic technique," Medical physics **38**, 6407–6415 (2011).
[3] P. Zhang, T. Li, J. Zhu, X. Zhu, S. Yang, Y. Wang, X. Yin, and X. Zhang, "Generation of acoustic self-bending and bottle beams by phase engineering," Nature communications **5**, 1–9 (2014).
[4] K. Melde, A. G. Mark, T. Qiu, and P. Fischer, "Holograms for acoustics," Nature **537**, 518–522 (2016).
[5] M. Brown, D. Nikitichev, B. Treeby, and B. Cox, "Generating arbitrary ultrasound fields with tailored optoacoustic surface profiles," Applied Physics Letters **110**, 094102 (2017).
[6] M. D. Brown, B. T. Cox, and B. E. Treeby, "Design of multi-frequency acoustic kinoforms," Applied Physics Letters **111**, 244101 (2017).
[7] M. D. Brown, J. Jaros, B. T. Cox, and B. E. Treeby, "Control of broadband optically generated ultrasound pulses using binary amplitude holograms," The Journal of the Acoustical Society of America **139**, 1637–1647 (2016).
[8] N. Jiménez, V. Romero-García, L. M. García-Raffi, F. Camarena, and K. Staliunas, "Sharp acoustic vortex focusing by fresnel-spiral zone plates," Applied Physics Letters **112**, 204101 (2018).
[9] Y. Xie, C. Shen, W. Wang, J. Li, D. Suo, B.-I. Popa, Y. Jing, and S. A. Cummer, "Acoustic holographic rendering with two-dimensional metamaterial-based passive phased array," Scientific reports **6**, 1–6 (2016).
[10] Y. Tian, Q. Wei, Y. Cheng, and X. Liu, "Acoustic holography based on composite metasurface with decoupled modulation of phase and amplitude," Applied Physics Letters **110**, 191901 (2017).
[11] G. Memoli, M. Caleap, M. Asakawa, D. R. Sahoo, B. W. Drinkwater, and S. Subramanian, "Metamaterial bricks and quantization of meta-surfaces," Nature communications **8**, 1–8 (2017).
[12] Y. Zhu, J. Hu, X. Fan, J. Yang, B. Liang, X. Zhu, and J. Cheng, "Fine manipulation of sound via lossy metamaterials with independent and arbitrary reflection amplitude and phase," Nature communications **9**, 1–9 (2018).
[13] A. Marzo, S. A. Seah, B. W. Drinkwater, D. R. Sahoo, B. Long, and S. Subramanian, "Holographic acoustic elements for manipulation of levitated objects," Nature communications **6**, 1–7 (2015).
[14] M. A. Norasikin, D. Martinez Plasencia, S. Polychronopoulos, G. Memoli, Y. Tokuda, and S. Subramanian, "Soundbender: dynamic acoustic control behind obstacles," in *Proceedings of the 31st Annual ACM Symposium on User Interface Software and Technology* (2018) pp. 247–259.
[15] N. Jiménez, J.-P. Groby, and V. Romero-García, "Spiral sound-diffusing metasurfaces based on holographic vortices," Scientific reports **11**, 1–13 (2021).
[16] K. Melde, E. Choi, Z. Wu, S. Palagi, T. Qiu, and P. Fischer, "Acoustic fabrication via the assembly and fusion of particles," Advanced Materials **30**, 1704507 (2018).
[17] T. Fushimi, A. Marzo, B. W. Drinkwater, and T. L. Hill, "Acoustophoretic volumetric displays using a fast-moving levitated particle," Applied Physics Letters **115**, 064101 (2019).
[18] P. Kruizinga, P. van der Meulen, A. Fedjajevs, F. Mastik, G. Springeling, N. de Jong, J. G. Bosch, and G. Leus, "Compressive 3d ultrasound imaging using a single sensor," Science advances **3**, e1701423 (2017).
[19] G. Maimbourg, A. Houdouin, T. Deffieux, M. Tanter, and J.-F. Aubry, "3d-printed adaptive acoustic lens as a disruptive technology for transcranial ultrasound therapy using single-element transducers," Physics in Medicine & Biology **63**, 025026 (2018).
[20] S. Jiménez-Gambín, N. Jiménez, J. M. Benlloch, and F. Camarena, "Holograms to focus arbitrary ultrasonic fields through the skull," Physical Review Applied **12**, 014016 (2019).
[21] D. Andrés, N. Jiménez, J. M. Benlloch, and F. Camarena, "Numerical study of acoustic holograms for deep-brain targeting through the temporal-bone windowy," Ultrasound in Medicine and Biology **In Press**, – (2021).
[22] S. Jiménez-Gambín, N. Jiménez, and F. Camarena, "Transcranial focusing of ultrasonic vortices by acoustic holograms," Physical Review Applied **14**, 054070 (2020).
[23] Z. Ma, A. W. Holle, K. Melde, T. Qiu, K. Poeppel, V. M. Kadiri, and P. Fischer, "Acoustic holographic cell patterning in a biocompatible hydrogel," Advanced Materials **32**, 1904181 (2020).
[24] J. Kim, S. Kasoji, P. G. Durham, and P. A. Dayton, "Acoustic holograms for directing arbitrary cavitation patterns," Applied Physics Letters **118**, 051902 (2021).
[25] S. Jimenez-Gambin, N. Jimenez, A. Pouliopoulos, J. M. Benlloch, E. E. Konofagou, and F. Camarena, "Acoustic holograms for bilateral blood-brain barrier opening in a mouse model," IEEE Transactions on Biomedical Engineering (2021).
[26] A. Randad, M. A. Ghanem, M. R. Bailey, and A. D. Maxwell, "Design, fabrication, and characterization of broad beam transducers for fragmenting large renal calculi with burst wave lithotripsy," The Journal of the Acoustical Society of America **148**, 44–50 (2020).
[27] T. L. Szabo, *Diagnostic ultrasound imaging: inside out* (Academic press, 2004).
[28] J.-M. Escoffre and A. Bouakaz, *Therapeutic ultrasound*, Vol. 880 (Springer, 2015).
[29] A. Blana, B. Walter, S. Rogenhofer, and W. F. Wieland, "High-intensity focused ultrasound for the treatment of localized prostate cancer: 5-year experience," Urology **63**, 297–300 (2004).
[30] S. Toraya-Brown and S. Fiering, "Local tumour hyperthermia as immunotherapy for metastatic cancer," International journal of hyperthermia **30**, 531–539 (2014).
[31] M. Mallory, E. Gogineni, G. C. Jones, L. Greer, and C. B. Simone II, "Therapeutic hyperthermia: The old, the new, and the upcoming," Critical reviews in oncology/hematology **97**, 56–64 (2016).
[32] M. D. Gray, P. C. Lyon, C. Mannaris, L. K. Folkes, M. Stratford, L. Campo, D. Y. Chung, S. Scott, M. Anderson, R. Goldin, *et al.*, "Focused ultrasound hyperthermia for targeted drug release from thermosensitive liposomes: results from a phase i trial," Radiology **291**, 232–238 (2019).
[33] F. Mohamed, P. Marchettini, O. A. Stuart, M. Urano, and P. H. Sugarbaker, "Thermal enhancement of new chemotherapeutic agents at moderate hyperthermia," Annals of surgical oncology **10**, 463–468 (2003).
[34] R. Staruch, R. Chopra, and K. Hynynen, "Hyperthermia in bone generated with mr imaging–controlled focused ultrasound: Control strategies and drug delivery," Radiology **263**, 117–127 (2012).
[35] M. Tillander, S. Hokland, J. Koskela, H. Dam, N. P. Andersen, M. Pedersen, K. Tanderup, M. Ylihautala, and M. Köhler, "High intensity focused ultrasound induced in vivo large volume hyperthermia under 3d mri temperature control," Medical physics **43**, 1539–1549 (2016).
[36] C. Bing, R. M. Staruch, M. Tillander, M. O. Köhler, C. Mougenot, M. Ylihautala, T. W. Laetsch, and R. Chopra, "Drift correction for accurate prf-shift mr thermometry during mild hyperthermia treatments with mr-hifu," International Journal of Hyperthermia **32**, 673–687 (2016).
[37] N. Farr, Y.-N. Wang, S. D?Andrea, F. Starr, A. Partanen, K. M. Gravelle, J. S. McCune, L. J. Risler, S. G. Whang, A. Chang, *et al.*, "Hyperthermia-enhanced targeted drug delivery using magnetic resonance-guided focussed ultrasound: a pre-clinical study in a genetic model of pancreatic cancer," International Journal of Hyperthermia **34**, 284–291 (2018).
[38] R. L. Mcintosh and V. Anderson, "A comprehensive tissue properties database provided for the thermal assessment of a human at rest," Biophysical Reviews and Letters **5**, 129–151 (2010).
[39] B. E. Hammer, "Physical properties of tissues," Radiology **181**, 128–128 (1991).
[40] B. E. Treeby, J. Jaros, A. P. Rendell, and B. Cox, "Modeling nonlinear ultrasound propagation in heterogeneous media with power law absorption using ak-space pseudospectral method," The Journal of the Acoustical So-

ciety of America **131**, 4324–4336 (2012).
[41]H. H. Pennes, "Analysis of tissue and arterial blood temperatures in the resting human forearm," Journal of applied physiology **1**, 93–122 (1948).
[42]The parameters for the MRI acquisition were TR/TE = 55/10 ms, 25-deg flip angle, 300 mm × 300 mm × 4 mm volume, 128 × 128 acquisition matrix using an in-plane pixel size of 2.3 mm, 6/8 Fourier reconstruction and 260-Hz/px bandwidth.
[43]See a video of the IR-camera measurements in the supplementary material.
[44]See a video of the MRI-thermometry measurements in the supplementary material.
[45]MRI acquisition parameters: TR/TE = 42/10 ms, 300 mm × 300 mm × 6 mm, 128 × 128 acq. matrix (with 2.3-mm in-plane pixel size), 25-deg flip angle, 6/8 partial Fourier acquisition, 260-Hz/px bandwidth.